AIP | The Journal of Chemical Physics

# Electronic and thermoelectric properties of few-layer transition metal dichalcogenides

Darshana Wickramaratne, Ferdows Zahid, and Roger K. Lake

Citation: The Journal of Chemical Physics **140**, 124710 (2014); doi: 10.1063/1.4869142
View online: http://dx.doi.org/10.1063/1.4869142
View Table of Contents: http://scitation.aip.org/content/aip/journal/jcp/140/12?ver=pdfcov
Published by the AIP Publishing

**Articles you may be interested in**

Strain and electric field induced electronic properties of two-dimensional hybrid bilayers of transition-metal dichalcogenides
J. Appl. Phys. **116**, 063711 (2014); 10.1063/1.4892798

Computational study on electrical properties of transition metal dichalcogenide field-effect transistors with strained channel
J. Appl. Phys. **115**, 034505 (2014); 10.1063/1.4861726

Enhancement of band-to-band tunneling in mono-layer transition metal dichalcogenides two-dimensional materials by vacancy defects
Appl. Phys. Lett. **104**, 023512 (2014); 10.1063/1.4862667

Two-dimensional semiconductor alloys: Monolayer Mo1−xWxSe2
Appl. Phys. Lett. **104**, 012101 (2014); 10.1063/1.4834358

Performance limits of transition metal dichalcogenide (MX2) nanotube surround gate ballistic field effect transistors
J. Appl. Phys. **113**, 194502 (2013); 10.1063/1.4805059

This article is copyrighted as indicated in the article. Reuse of AIP content is subject to the terms at: http://scitation.aip.org/termsconditions. Downloaded to IP: 147.8.204.164 On: Tue, 02 Dec 2014 09:15:56

THE JOURNAL OF CHEMICAL PHYSICS 140, 124710 (2014)

# Electronic and thermoelectric properties of few-layer transition metal dichalcogenides

Darshana Wickramaratne,[1] Ferdows Zahid,[2] and Roger K. Lake[1]
[1] *Department of Electrical Engineering, University of California, Riverside, California 92521-0204, USA*
[2] *Department of Physics and the Center of Theoretical and Computational Physics, The University of Hong Kong, Pokfulam Road, Hong Kong SAR, China*

(Received 2 January 2014; accepted 7 March 2014; published online 31 March 2014)

The electronic and thermoelectric properties of one to four monolayers of $MoS_2$, $MoSe_2$, $WS_2$, and $WSe_2$ are calculated. For few layer thicknesses, the near degeneracies of the conduction band $K$ and $\Sigma$ valleys and the valence band $\Gamma$ and $K$ valleys enhance the n-type and p-type thermoelectric performance. The interlayer hybridization and energy level splitting determine how the number of modes within $k_BT$ of a valley minimum changes with layer thickness. In all cases, the maximum ZT coincides with the greatest near-degeneracy within $k_BT$ of the band edge that results in the sharpest turn-on of the density of modes. The thickness at which this maximum occurs is, in general, not a monolayer. The transition from few layers to bulk is discussed. Effective masses, energy gaps, power-factors, and ZT values are tabulated for all materials and layer thicknesses. © *2014 AIP Publishing LLC*. [http://dx.doi.org/10.1063/1.4869142]

## I. INTRODUCTION

Semiconducting, transition-metal dichalcogenides (TMDCs) exhibit promising electronic,[1–5] opto-electronic,[6] and spintronic[7] properties. Single monolayers (three atomic layers) can be either exfoliated or grown with chemically stable surfaces. The electronic, optical, and spin properties of monolayers are qualitatively different from those of the bulk. The bandgap changes from indirect to direct, and the valence band edges at the $K$ and $K'$ points become spin polarized.[6,7] These materials are discussed in a number of recent reviews.[8–12]

Experimental studies conducted on a different set of two-dimensional materials, namely, $Bi_2Te_3$ and $Bi_2Se_3$, demonstrated an improvement in their thermoelectric performance as their thickness was reduced.[13,14] A large increase in ZT has been theoretically predicted for monolayer $Bi_2Te_3$ compared to that of the bulk.[15–17] This enhancement in ZT results from the unique, step-function shape of the density of modes at the valence band edge of a single quintuple layer.[16,17] The shape of the density of modes increases the power factor, and the increase in the power factor increases ZT. For $Bi_2Te_3$, the large enhancement in the power factor and in ZT only occurs for a monolayer. For bilayer and trilayer $Bi_2Te_3$, the step-like shape of the density of modes disappears, and the calculated values of ZT are either slightly higher[18] or slightly lower[17] than that of the bulk.

Prior experimental and theoretical investigations of the thermoelectric performance of transition metal dichalcogenides have focused on either bulk or monolayer materials.[6,19–24] There has not been a study of the effect of film thickness on the power factor and ZT in the transition metal dichalcogenides. It is not known whether the power factor and ZT are maximum at monolayer thickness or at some other thickness.

This work theoretically investigates the electronic properties and the thermoelectric performance of bulk and one to four monolayers of 4 different TMDC materials: $MoS_2$, $MoSe_2$, $WS_2$, and $WSe_2$. The goal is to understand how their electronic and thermoelectric properties vary with thickness. Similar to monolayer $Bi_2Te_3$, the increase in ZT for the ultrathin films results from an enhanced degeneracy or near-degeneracy of the band edges. In the TMDCs, at few layer thicknesses, different valleys become nearly degenerate with energy differences of less than $k_BT$ at room temperature. Because of weak interlayer coupling at certain valleys, additional bands from additional layers lie within $k_BT$ of the band edges for few layer thicknesses. The increased degeneracy results in a sharper turn on of the density of modes near the band edges. In all cases, the thickness with the sharpest increase in the density of modes has the largest value for ZT. For the semiconducting TMDCs considered here, that optimum thickness is not, in general, a single monolayer.

## II. THEORETICAL METHODS

*Ab initio* calculations of the bulk and few-layer structures (one to four layers) are carried out using density functional theory (DFT) with a projector augmented wave method[25] and the Perdew-Burke-Ernzerhof (PBE) type generalized gradient approximation[26,27] as implemented in the Vienna *ab initio* simulation package (VASP).[28,29] The vdW interactions in $MoSe_2$ and $MoS_2$ are accounted for using a semi-empirical correction to the Kohn-Sham energies when optimizing the bulk structures (optimization of $WS_2$ and $WSe_2$ structures are done at the PBE level since the semi-empirical parameters for tungsten are currently not described by the dispersion potential).[30] The Monkhorst-Pack scheme is used for the integration of the Brillouin zone with a k-mesh of 12 × 12

 © 2014 AIP Publishing LLC

This article is copyrighted as indicated in the article. Reuse of AIP content is subject to the terms at: http://scitation.aip.org/termsconditions. Downloaded to IP: 147.8.204.164 On: Tue, 02 Dec 2014 09:15:56

$\times$ 6 for the bulk structures and 12 $\times$ 12 $\times$ 1 for the thin films. The energy cutoff of the plane wave basis is 300 eV. All of the electronic band structure calculations include spin-orbit coupling. Calculations are also performed without spin-orbit coupling and the results are compared.

To verify the results of the PBE calculations, the electronic structure of 1L, 2L, 3L, and 4L $MoS_2$ are calculated using the much more computationally expensive hybrid Heyd-Scuseria-Ernzerhof (HSE) functional.[31] The HSE calculations incorporate 25% short-range Hartree-Fock exchange. The screening parameter $\mu$ is set to 0.4 Å$^{-1}$.

The thermoelectric parameters are calculated from a Landauer formalism using the *ab initio* derived density of modes.[16,17,23] In the linear response regime, the electronic conductivity ($\sigma$), the electronic thermal conductivity ($\kappa_e$), and the Seebeck coefficient (S) are expressed as[32,33]

$$\sigma = (2q^2/h)I_0 \quad (\Omega^{-1}\text{m}^{-1}), \tag{1}$$

$$\kappa_e = \left(2Tk_B^2/h\right)\left(I_2 - I_1^2/I_0\right) \quad (\text{Wm}^{-1}\,\text{K}^{-1}), \tag{2}$$

$$S = -(k_B/q)\frac{I_1}{I_0} \quad (\text{V/K}), \tag{3}$$

with

$$I_j = \frac{1}{L}\int_{-\infty}^{\infty}\left(\frac{E-E_F}{k_BT}\right)^j \bar{T}(E)\left(-\frac{\partial f_0}{\partial E}\right)dE, \tag{4}$$

where $L$ is the device length, $q$ is the magnitude of the electron charge, $h$ is Planck's constant, and $k_B$ is Boltzmann's constant. The transmission function is

$$\bar{T}(E) = T(E)M(E), \tag{5}$$

where M(E) as the density of modes (DOM). In the diffusive limit,

$$T(E) = \lambda(E)/L, \tag{6}$$

and $\lambda(E)$ is the electron mean free path. When phonon scattering is dominant, the mean free path can be written as a constant, $\lambda(E) = \lambda_0$. As discussed in Ref. 34, the transport distribution, $\Xi(E)$, arising from the Boltzmann transport equation is related to the above quantities by $\Xi(E) = \frac{2}{h}T(E)M(E)$.

The density of modes M(E) can be defined as[17,32]

$$M(E) = \left(\frac{L_\perp}{2\pi}\right)^{d-1}\int_{BZ}\sum_{k_\perp}\Theta(E-\epsilon(k_\perp))dk_\perp^{d-1}, \tag{7}$$

where $d$ is the dimensionality of the system, $L_\perp$ are the dimensions of the structure perpendicular to the direction of transport ($L_\perp^2$ = W $\times$ t for d = 3, $L_\perp$ = W for d = 2; W = width of the structure, t = film thickness), $\Theta$ is the unit step function, and $k_\perp$ refers to the $k$ states in the first Brillouin zone perpendicular to the transport direction. Using Eq. (7), M(E) of any material in any dimension can be numerically evaluated from a given electronic band structure by counting the bands that cross the energy of interest. The density of modes calculations are performed by integrating over the first Brillouin zone using a converged k point grid (51 $\times$ 51 $\times$ 10 k points for the bulk structures and 51 $\times$ 51 $\times$ 1 for the thin films).

We account for carrier scattering within each structure by fitting our calculated bulk electrical conductivity with bulk experimental data. An electron mean free path of $\lambda_0 = 14$ nm gives the best agreement with experimental data on the Seebeck response of bulk $MoS_2$ as a function of the electrical conductivity.[35,36] The bulk p-type electrical conductivity of $MoS_2$ at room temperature was reported to be 5.1 $\Omega^{-1}$ cm$^{-1}$ with a Seebeck coefficient of $\sim$450 $\mu$VK$^{-1}$ at a carrier concentration of $10^{16}$ cm$^{-3}$.[36] Using $\lambda_0 = 14$ nm we obtain an electrical conductivity of 4.97 $\Omega^{-1}$ cm$^{-1}$ with a Seebeck coefficient of $\sim$398 $\mu$VK$^{-1}$ at the same carrier concentration. This value of the mean free path is also consistent with a theoretically derived energy independent acoustic phonon-limited mean free path ($\lambda_0$ = 14 nm) for electrons in monolayer $MoS_2$,[37] and was successfully used to simulate and compare to experimental results of the transfer characteristics of single layer $MoS_2$ field effect transistor.[2] As an initial approximation of carrier scattering we use the same $\lambda_0$ value to model the thermoelectric properties of all the TMDC materials investigated in this study.

For the in-plane lattice thermal conductivity, a $\kappa_l$ value of 19.5 Wm$^{-1}$ K$^{-1}$ obtained from a molecular dynamics simulation on monolayer $MoS_2$ is used.[38] Prior experimental[39] and theoretical[23] studies of the lattice thermal conductivity in the TMDC materials have demonstrated that $\kappa_L$ does not vary significantly for the different TMDC compounds studied here. With the above quantities in hand, the power factor, $S^2\sigma$, and the thermoelectric figure of merit $ZT = S^2\sigma T/(\kappa_l + \kappa_e)$ are determined.

## III. RESULTS

All of the thermoelectric parameters are derived from the calculated electronic band structures. Therefore, we begin this section with a discussion of the calculated band structures. The band structure calculations produce considerably more information than is required for calculating the thermoelectric parameters. To preserve that information and contribute towards a database of material parameters, extracted properties such as effective masses and energy gaps at high symmetry points are tabulated.

Figure 1 shows the *ab initio* band structure of one-layer (1L) through four-layer (4L) and bulk $WS_2$. The large valence band splitting at the *K*-point and the direct-indirect gap transition as the film thickness increases above 1L are features that occur in the other TMDC materials included as part of this study. The last panel in Fig. 1 illustrates the effect of decreasing layer thickness on the bandgap for all of the materials studied. The optimized lattice parameters of the bulk TMDC compounds are listed in Table I. The results in Table I and Figure 1 are consistent with prior experimental characterization[40–42] and theoretical calculations of the bulk[43,44] and thin film[46,47] crystal structures and electronic band structures. The results of these electronic structure calculations at the high symmetry points are summarized in Tables II and III. Table II gives the relative effective masses, and Table III gives the energy gaps.

A number of prior theoretical studies of the electronic structure of monolayer and few-layer TMDCs did not include

This article is copyrighted as indicated in the article. Reuse of AIP content is subject to the terms at: http://scitation.aip.org/termsconditions. Downloaded to IP: 147.8.204.164 On: Tue, 02 Dec 2014 09:15:56

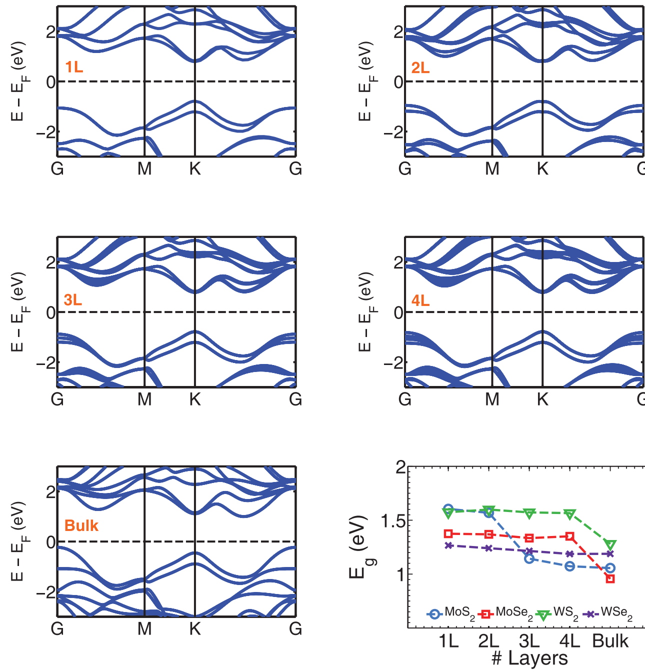


FIG. 1. *Ab initio* calculated band structures of $WS_2$: 1L, 2L, 3L, 4L, and bulk. The bottom right panel illustrates the variation of the bandgap of the TMDC materials as a function of the number of layers.

spin-orbit interaction.[45–47] As a result, the bandgaps reported in those studies are slightly larger. For example, the bandgaps reported in a prior PBE level calculation[47] are greater by 70 meV, 260 meV, and 284 meV for $MoS_2$ and $MoSe_2$, $WS_2$, and $WSe_2$, respectively, when compared to our calculation results. Without the inclusion of spin-orbit interaction, our values for the bandgap of the monolayer TMDCs are consistent with the bandgaps reported in these studies. Including spin-orbit coupling results in a splitting of the valence bands, $\Delta_{SO}$, at $K$. The spin orbit interaction shifts up one of the degenerate valence bands, and this reduces the bandgap. The degree of the energy shift ranges from 39.6 meV for $MoS_2$ to 210.9 meV for $WS_2$. The second degenerate valence band is shifted down by an energy that is also unique to each TMDC material; this ranges from 110.4 meV for $MoS_2$ to 316.2 meV for $WSe_2$. For example, the calculated $\Delta_{SO}$ energies of the monolayer TMDCs are 150 meV, 181 meV, 425 meV, and 461 meV for $MoS_2$, $MoSe_2$, $WS_2$, and $WSe_2$, respectively. This is in good agreement with a prior PBE level calculation[48] that accounted for spin-orbit interaction which obtained $\Delta_{SO}$ values of 146 meV, 183 meV, 425 meV, and 461 meV for $MoS_2$, $MoSe_2$, $WS_2$, and $WSe_2$, respectively, and a $\Delta_{SO}$ energy of 188 meV obtained for monolayer $MoS_2$ with the use of optical absorption experiments.[49]

More sophisticated many-body *ab initio* calculations which include HSE or GW calculations have been reported in prior studies of the band structure of monolayer[48,50,51,53] and bilayer[51,53] structures of the molybdenum and tungsten dichalcogenides. The values for $\Delta_{SO}$ resulting from these theories are only slightly changed from those of the PBE model. The $\Delta_{SO}$ values reported for monolayer $MoS_2$, $MoSe_2$, $WS_2$, and $WSe_2$ with a GW (HSE) calculation are 164 (193) meV, 212 (261) meV, 456 (521) meV, and 501 (586) meV.[48] The primary difference between the PBE and the HSE and GW calculations is an increase in the bandgap. However, the PBE bandgap is large enough compared to the temperatures considered that the exact magnitude of the bandgap has no effect on the thermoelectric parameters. An explicit comparison of the electronic structure and the thermoelectric parameters calculated from the PBE and the HSE functionals for 1L - 4L $MoS_2$ is given below.

Calculation of the thermoelectric parameters requires the density of modes extracted from the electronic band structure using Eq. (7). Figure 2 shows the density of modes versus energy for bulk, 1L, 2L, 3L, and 4L $MoS_2$, $MoSe_2$, $WS_2$, and $WSe_2$. To compare the density of modes of the bulk structure with the thin-film structures, we divide the density of modes of the thin-film structures by their respective thickness, $t$. As will be shown, for these TMDCs, small variations in the shape of the density of modes near the band edges can enhance the power factor and subsequently ZT. The thermoelectric properties of the bulk and thin-film structures are calculated from Eqs. (1)–(6) using the density of modes shown in Fig. 2.

The Seebeck coefficient, electrical conductivity, power-factor (PF), and the thermoelectric figure-of-merit (ZT) as a function of the reduced Fermi level, $\eta_F$ are shown in Figures 3–6, respectively. The reduced Fermi-level is $\eta_F = \frac{E_F - E_{C1}}{kT}$ for electrons in the conduction band, and $\eta_F = \frac{E_F - E_{V1}}{kT}$ for holes in the valence band. $E_{C1}$ and $E_{V1}$ are the energies of the conduction and valence band edges, respectively. For each material and each thickness the maximum power factor and ZT occurs for the conduction band states. The peak conduction band and valence band power factor and ZT for each structure and material at 77 K, 150 K, and 300 K are summarized in Tables IV and V, respectively. For all materials, the few layer structures show a large increase in the values of their power factor and ZT compared to those of the bulk.

The peak n-type ZT values (and corresponding layer thicknesses) for $MoS_2$, $MoSe_2$, $WS_2$, and $WSe_2$ are 2.23

TABLE I. Calculated properties of bulk TMDC materials: lattice constant $a_0$, c-axis lattice constant $c_0$, z-parameter $z$, and bandgap $E_g$(eV). Experimental values[40–42] have been included for comparison.

| | $a_0$(Å) | $c_0$(Å) | $z$ | $a_0^{expt}$(Å) | $c_0^{expt}$(Å) | $z^{expt}$ | $E_g$(eV) | $E_g^{expt}$(eV) |
|---|---|---|---|---|---|---|---|---|
| $MoS_2$ | 3.179 | 12.729 | 0.627 | 3.160 | 12.290 | 0.629 | 1.060 | 1.29 |
| $MoSe_2$ | 3.309 | 13.323 | 0.624 | 3.289 | 12.927 | 0.621 | 0.959 | 1.09 |
| $WS_2$ | 3.183 | 13.131 | 0.630 | 3.150 | 12.320 | 0.622 | 1.283 | 1.35 |
| $WSe_2$ | 3.319 | 13.729 | 0.627 | 3.282 | 12.960 | 0.621 | 1.188 | 1.20 |

This article is copyrighted as indicated in the article. Reuse of AIP content is subject to the terms at: http://scitation.aip.org/termsconditions. Downloaded to IP: 147.8.204.164 On: Tue, 02 Dec 2014 09:15:56

TABLE II. *Ab initio* calculations of the hole and electron effective masses at the valence band maxima and conduction band minima, respectively, for each structure in units of the free electron mass ($m_0$). The subscripts $l$ and $t$ refer to the masses calculated at the symmetry point along the longitudinal and the transverse directions.

| Structure | Point | $MoS_2$ | $MoSe_2$ | $WS_2$ | $WSe_2$ | $MoS_2$ | $MoSe_2$ | $WS_2$ | $WSe_2$ |
|---|---|---|---|---|---|---|---|---|---|
| | | **Hole effective mass ($m_0$)** | | | | **Electron effective mass ($m_0$)** | | | |
| 1L | $K_l$ | 0.543 | 0.578 | 0.339 | 0.341 | 0.506 | 0.502 | 0.349 | 0.345 |
| | $K_t$ | 0.546 | 0.588 | 0.339 | 0.348 | 0.504 | 0.503 | 0.347 | 0.345 |
| 2L | Γ | 1.039 | 1.430 | 1.239 | 1.322 | ... | ... | ... | ... |
| | $K_l$ | 0.548 | 0.595 | 0.345 | 0.349 | 0.521 | 0.539 | 0.359 | 0.411 |
| | $K_t$ | 0.546 | 0.596 | 0.346 | 0.348 | 0.510 | 0.539 | 0.359 | 0.412 |
| 3L | Γ | 1.239 | 1.432 | 1.246 | 1.382 | ... | ... | ... | ... |
| | $K_t$ | 0.549 | 0.602 | 0.366 | 0.368 | 0.559 | 0.544 | 0.376 | 0.434 |
| | $K_t$ | 0.548 | 0.604 | 0.366 | 0.368 | 0.559 | 0.544 | 0.377 | 0.434 |
| 4L | Γ | 1.239 | 1.433 | 1.351 | 1.432 | ... | ... | ... | ... |
| | $K_l$ | 0.548 | 0.604 | 0.366 | 0.367 | 0.554 | 0.542 | 0.376 | 0.435 |
| | $K_t$ | 0.546 | 0.604 | 0.366 | 0.368 | 0.559 | 0.549 | 0.377 | 0.434 |
| Bulk | Γ | 0.838 | 0.973 | 0.832 | 0.997 | ... | ... | ... | ... |
| | $\Sigma_l$ | ... | ... | ... | ... | 0.590 | 0.521 | 0.569 | 0.489 |
| | $\Sigma_t$ | ... | ... | ... | ... | 0.845 | 0.776 | 0.665 | 0.643 |

(t = 3L), 2.39 (t = 2L), 2.03 (t = 3L), and 1.91 (t = 2L) which is an improvement by a factor of 6.4, 8.2, 7.2, and 7.5 over the respective bulk values. These peak ZT values occur when the Fermi level is moved by 1.39 kT, 1.55 kT, 1.08 kT, and 1.39 kT, respectively, below the conduction band at T = 300 K. This corresponds to electron carrier densities of $6.26 \times 10^{19}$ cm$^{-3}$, $5.74 \times 10^{19}$ cm$^{-3}$, $5.34 \times 10^{19}$ cm$^{-3}$, and $4.72 \times 10^{19}$ cm$^{-3}$ for $MoS_2$, $MoSe_2$, $WS_2$, and $WSe_2$, respectively. The peak p-type ZT values (and corresponding layer thicknesses) for $MoS_2$, $MoSe_2$, $WS_2$, and $WSe_2$ are 1.15 (t = 2L), 0.81 (t = 2L-4L), 0.76 (t = 2L-3L), and 0.62 (t = 1L-4L) which is an improvement by a factor of 14.4, 10.1, 9.5, and 5.2 over the respective bulk values. These peak ZT values occur when the Fermi level is moved by 1.16 kT, 1.01 kT, 0.93 kT, and 0.85 kT, respectively, above the valence band at T = 300 K. This corresponds to hole carrier densities

TABLE III. *Ab initio* calculations of the bandgap energies and energy transitions between the valence ($v$) and conduction ($c$) band valleys for each structure and material. The splitting of the valence band at the $K$-point due to spin-orbit coupling and the inter-layer interactions are denoted as $K_{v1}$ and $K_{v2}$. Σ is the mid-point between Γ and $K$. The bandgap at each dimension is highlighted in bold text. Experimental values when available[40–42,59] have been included for comparison. (Note: The bandgap of 2L, 3L, and 4L $WSe_2$ occurs between the $K_{v1}$ and $\Sigma_C$. The 2L, 3L, and 4L bandgaps of $WSe_2$ are 1.216 eV, 1.1594 eV, and 1.1345 eV, respectively.)

| Structure | Transition | $MoS_2$ | $MoSe_2$ | $WS_2$ | $WSe_2$ | $MoS_2$ | $MoSe_2$ | $WS_2$ | $WSe_2$ |
|---|---|---|---|---|---|---|---|---|---|
| | | **Calculated (eV)** | | | | **Expt. (eV)** | | | |
| 1L | $\Gamma_v$ to $K_c$ | 1.705 | 1.768 | 1.849 | 1.776 | ... | ... | ... | ... |
| | $\Gamma_v$ to $\Sigma_c$ | 1.922 | 1.862 | 1.929 | 1.806 | ... | ... | ... | ... |
| | $K_{v1}$ to $K_c$ | **1.600** | **1.375** | **1.573** | **1.254** | 1.900 | 1.660 | 1.950 | 1.640 |
| | $K_{v2}$ to $K_c$ | 1.750 | 1.556 | 1.973 | 1.715 | 2.050 | 1.850 | 2.360 | 2.040 |
| 2L | $\Gamma_v$ to $K_c$ | **1.564** | **1.368** | **1.507** | 1.586 | 1.600 | ... | 1.730 | ... |
| | $\Gamma_v$ to $\Sigma_c$ | 1.775 | 1.373 | 1.542 | 1.562 | ... | ... | ... | ... |
| | $K_{v1}$ to $K_c$ | 1.600 | 1.373 | 1.549 | 1.269 | 1.880 | ... | 1.910 | 1.590 |
| | $K_{v2}$ to $K_c$ | 1.760 | 1.556 | 1.977 | 1.788 | 2.050 | ... | 2.340 | 2.000 |
| 3L | $\Gamma_v$ to $K_c$ | **1.150** | **1.334** | **1.458** | 1.586 | ... | ... | ... | ... |
| | $\Gamma_v$ to $\Sigma_c$ | 1.171 | 1.372 | 1.482 | 1.508 | ... | ... | ... | ... |
| | $K_{v1}$ to $K_c$ | 1.620 | 1.376 | 1.485 | 1.265 | ... | ... | ... | ... |
| | $K_{v2}$ to $K_c$ | 1.780 | 1.564 | 1.873 | 1.783 | ... | ... | ... | ... |
| 4L | $\Gamma_v$ to $K_c$ | **1.120** | **1.351** | **1.438** | 1.546 | ... | ... | ... | ... |
| | $\Gamma_v$ to $\Sigma_c$ | 1.139 | 1.374 | 1.439 | 1.434 | ... | ... | ... | ... |
| | $K_{v1}$ to $K_c$ | 1.630 | 1.356 | 1.459 | 1.259 | ... | ... | ... | ... |
| | $K_{v2}$ to $K_c$ | 1.780 | 1.574 | 1.877 | 1.753 | ... | ... | ... | ... |
| Bulk | $\Gamma_v$ to $\Sigma_c$ | **1.060** | **0.959** | **1.283** | **1.188** | 1.290 | 1.090 | 1.350 | 1.200 |
| | $K_{v1}$ to $K_c$ | 1.590 | 1.349 | 1.453 | 1.258 | 1.880 | 1.350 | 1.880 | 1.580 |
| | $K_{v2}$ to $K_c$ | 1.780 | 1.588 | 1.889 | 1.737 | 2.060 | 1.380 | 2.320 | 1.950 |

This article is copyrighted as indicated in the article. Reuse of AIP content is subject to the terms at: http://scitation.aip.org/termsconditions. Downloaded to IP: 147.8.204.164 On: Tue, 02 Dec 2014 09:15:56

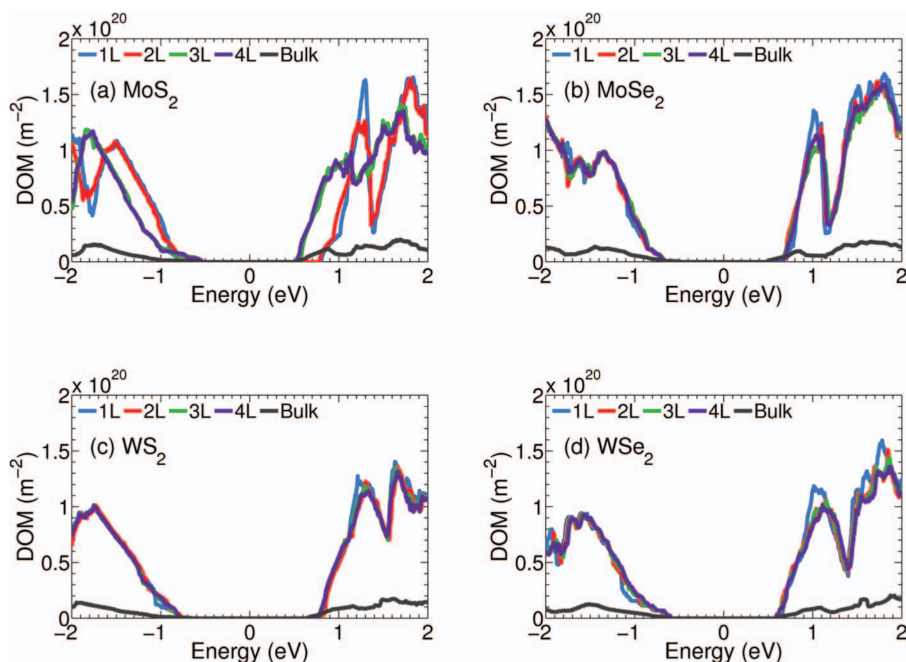


FIG. 2. Distribution of modes per unit area versus energy for (a) $MoS_2$, (b) $MoSe_2$, (c) $WS_2$, and (d) $WSe_2$ for bulk (black), 1L (blue), 2L (red), 3L (green), and 4L (purple) structures. The midgap energy is set to E = 0.

of $7.12 \times 10^{19}$ cm$^{-3}$, $5.84 \times 10^{19}$ cm$^{-3}$, $4.02 \times 10^{19}$ cm$^{-3}$, and $3.91 \times 10^{19}$ cm$^{-3}$ for $MoS_2$, $MoSe_2$, $WS_2$, and $WSe_2$, respectively. Of the four TMDC materials studied, $MoS_2$ is the only material to exhibit a p-type and n-type ZT > 1. In contrast to $Bi_2Te_3$, the peak value of ZT does not occur in any of the materials at a monolayer thickness.

The Seebeck coefficients at the maximum n-type (p-type) ZT for each material are 275 (245.6) $\mu$VK$^{-1}$, 287 (230.7) $\mu$VK$^{-1}$, 279 (230.1) $\mu$VK$^{-1}$, and 276 (216.7) $\mu$VK$^{-1}$ for $MoS_2$, $MoSe_2$, $WS_2$, and $WSe_2$, respectively. However, the Seebeck coefficients at the maximum n-type (p-type) power factor for each material are 167 (90.4) $\mu$VK$^{-1}$, 100 (185.8) $\mu$VK$^{-1}$, 165 (177.1) $\mu$VK$^{-1}$, and 171 (172.1) $\mu$VK$^{-1}$ for $MoS_2$, $MoSe_2$, $WS_2$, and $WSe_2$, respectively. This is generally consistent with the conclusion of a report on engineering the Seebeck coefficient to obtain the maximum thermoelectric power factor.[52]

Without the inclusion of spin-orbit interaction our values of the ballistic ZT for the monolayer TMDC materials are consistent with a prior report on the monolayer thermoelectric properties of these TMDC materials.[23] Our calculations show that without the inclusion of spin-orbit interaction the peak n-type ZT values for all materials continue to occur at thicknesses above a single monolayer. The peak

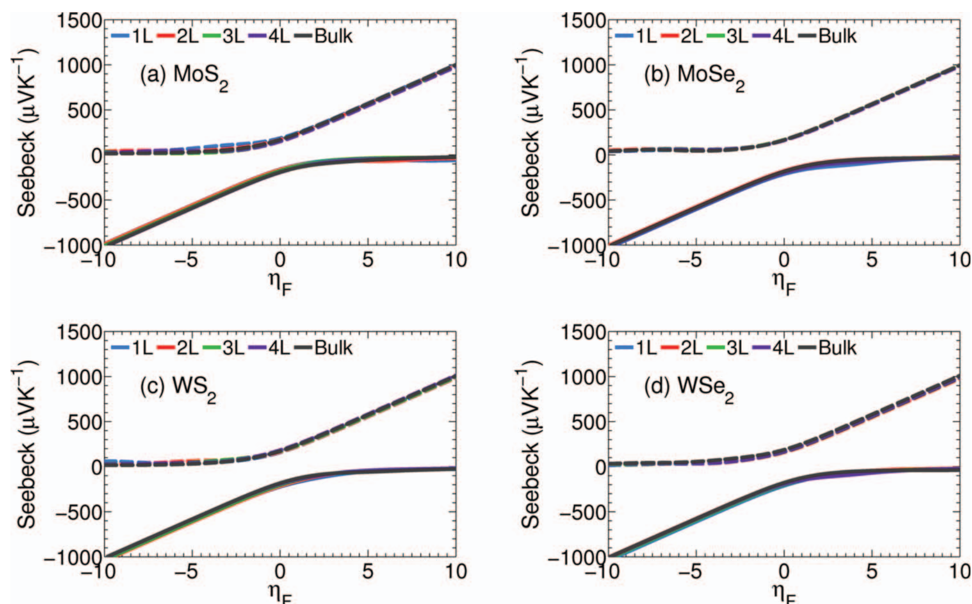


FIG. 3. Seebeck coefficient at 300 K for (a) $MoS_2$, (b) $MoSe_2$, (c) $WS_2$, and (d) $WSe_2$ for bulk (black), 1L (blue), 2L (red), 3L (green), and 4L (purple) structures. The n-type Seebeck coefficients are plotted with a solid line and p-type coefficients with a broken line as a function of the reduced Fermi energy, $\eta_F$.

This article is copyrighted as indicated in the article. Reuse of AIP content is subject to the terms at: http://scitation.aip.org/termsconditions. Downloaded to IP: 147.8.204.164 On: Tue, 02 Dec 2014 09:15:56

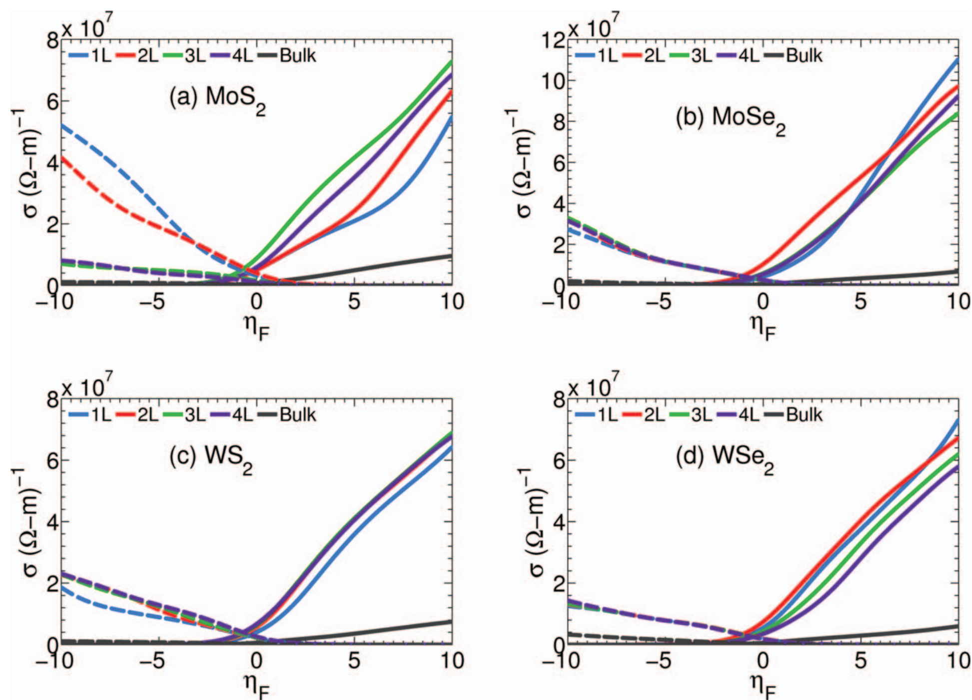


FIG. 4. Electrical conductivity, $\sigma$, at 300 K for (a) $MoS_2$, (b) $MoSe_2$, (c) $WS_2$, and (d) $WSe_2$ for 1L (blue), 2L (red), 3L (green), and 4L (purple) and bulk (black) structures. The n-type electrical conductivity is plotted with a solid line and p-type conductivity with a broken line as a function of the reduced Fermi energy, $\eta_F$.

n-type ZT values (and corresponding layer thicknesses) without spin-orbit interaction for $MoS_2$, $MoSe_2$, $WS_2$, and $WSe_2$ are 1.38 (t = 3L), 1.52 (t = 2L), 1.13 (t = 4L), and 1.28 (t = 2L). However, the peak p-type ZT values without spin-orbit interaction occurs for a single monolayer for each TMDC material. The p-type ZT values without spin-orbit interaction for $MoS_2$, $MoSe_2$, $WS_2$, and $WSe_2$ are 1.42, 0.84, 0.90, and 0.69.

Recent electronic structure calculations using the Heyd-Scuseria-Ernzerhof (HSE) hybrid functional[53] give a bandgap that more accurately matches known experimental values.[53] To assess whether the trends in the thermoelectric parameters predicted with the PBE functional are the same as those resulting from the HSE functional, we calculate the electronic band structure of 1L, 2L, 3L, and 4L $MoS_2$ with both the PBE and the HSE functional and plot the results in Fig. 7. Near the

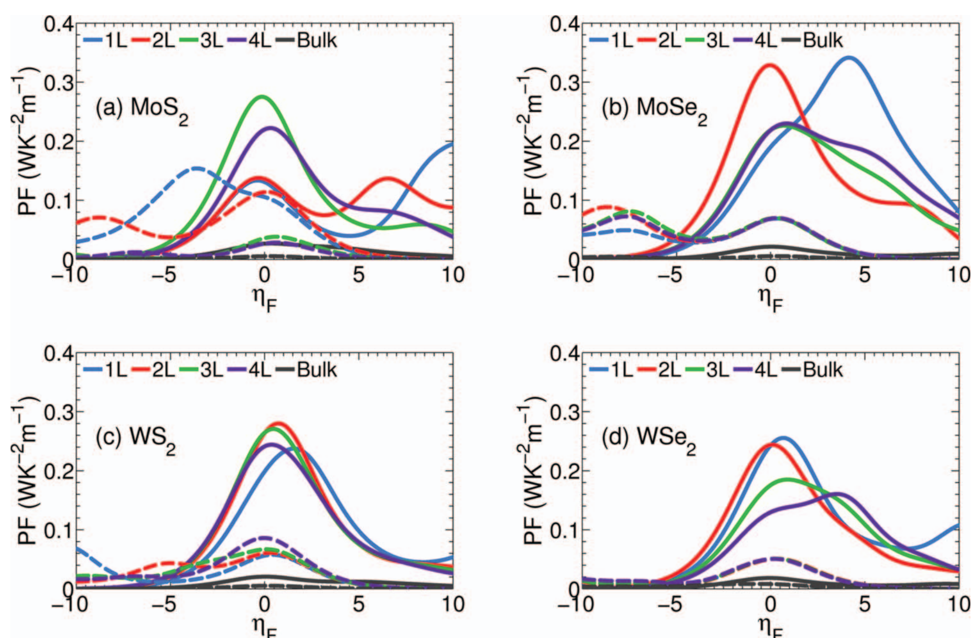


FIG. 5. Power factor (PF) at 300 K for (a) $MoS_2$, (b) $MoSe_2$, (c) $WS_2$, and (d) $WSe_2$ for bulk (black), 1L (blue), 2L (red), 3L (green), and 4L (purple) structures. The n-type power factors are plotted with a solid line and p-type PFs with a broken line as a function of the reduced Fermi energy, $\eta_F$.

This article is copyrighted as indicated in the article. Reuse of AIP content is subject to the terms at: http://scitation.aip.org/termsconditions. Downloaded to IP: 147.8.204.164 On: Tue, 02 Dec 2014 09:15:56

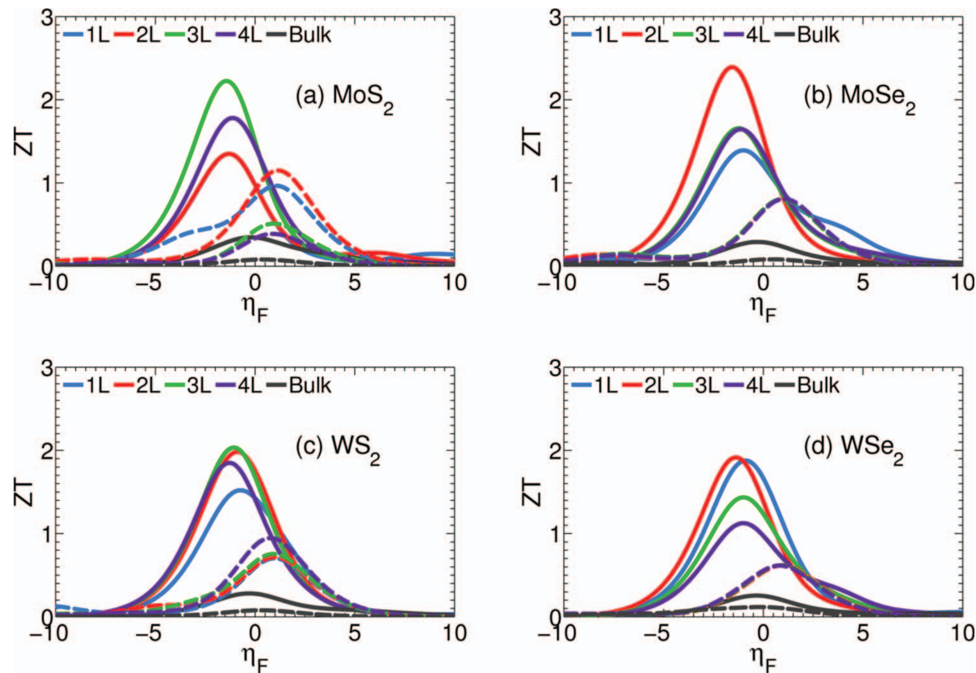


FIG. 6. ZT at 300 K for (a) $MoS_2$, (b) $MoSe_2$, (c) $WS_2$, and (d) $WSe_2$ for bulk (black), 1L (blue), 2L (red), 3L (green), and 4L (purple) structures. The n-type ZT is plotted with a solid line and p-type ZT with a broken line as a function of the reduced Fermi energy, $\eta_F$.

TABLE IV. Peak n-type (p-type) power factor of 1L, 2L, 3L, 4L and bulk $MoS_2$, $MoSe_2$, $WS_2$, and $WSe_2$ at 300 K, 150 K, and 77 K. The maximum power factor for each material at a given temperature is in bold.

| | Temperature | 1L | 2L | 3L | 4L | Bulk |
|---|---|---|---|---|---|---|
| | | **Maximum n-type (p-type) power factor (WK$^{-2}$ m$^{-2}$)** | | | | |
| $MoS_2$ | 300 K | 0.130 (0.150) | 0.140 (0.110) | **0.280** (0.041) | 0.220 (0.031) | 0.0320 (0.010) |
| | 150 K | 0.093 (0.072) | 0.093 (0.071) | **0.190** (0.032) | 0.120 (0.024) | 0.012 (0.0042) |
| | 77 K | 0.072 (0.043) | 0.072 (0.053) | **0.13** (0.021) | 0.063 (0.022) | 0.012 (0.0031) |
| $MoSe_2$ | 300 K | **0.340** (0.071) | 0.330 (0.094) | 0.230 (0.082) | 0.230 (0.071) | 0.022 (0.0061) |
| | 150 K | **0.151** (0.050) | 0.200 (0.051) | 0.100 (0.051) | 0.100 (0.052) | 0.013 (0.004) |
| | 77 K | **0.062** (0.031) | 0.120 (0.032) | 0.062 (0.031) | 0.052 (0.032) | 0.013 (0.0032) |
| $WS_2$ | 300 K | 0.240 (0.062) | **0.280** (0.061) | 0.270 (0.071) | 0.240 (0.092) | 0.022 (0.0052) |
| | 150 K | 0.110 (0.042) | **0.160** (0.042) | 0.150 (0.041) | 0.130 (0.051) | 0.010 (0.0043) |
| | 77 K | 0.051 (0.031) | **0.081** (0.032) | 0.070 (0.032) | 0.081 (0.031) | 0.010 (0.0022) |
| $WSe_2$ | 300 K | **0.260** (0.054) | 0.240 (0.052) | 0.190 (0.053) | 0.160 (0.053) | 0.022 (0.014) |
| | 150 K | **0.141** (0.030) | 0.140 (0.031) | 0.081 (0.031) | 0.070 (0.031) | 0.010 (0.004) |
| | 77 K | 0.071 (0.031) | **0.082** (0.031) | 0.050 (0.031) | 0.043 (0.022) | 0.011 (0.0021) |

TABLE V. Peak n-type (p-type) thermoelectric figure of merit, ZT, of 1L, 2L, 3L, 4L and bulk $MoS_2$, $MoSe_2$, $WS_2$, and $WSe_2$ at 300 K, 150 K, and 77 K. The maximum ZT for each material at a given temperature is in bold.

| | Temperature | 1L | 2L | 3L | 4L | Bulk |
|---|---|---|---|---|---|---|
| | | **Maximum n-type (p-type) ZT** | | | | |
| $MoS_2$ | 300 K | 1.35 (0.970) | 1.35 (1.15) | **2.23** (0.510) | 1.78 (0.390) | 0.350 (0.081) |
| | 150 K | 0.590 (0.350) | 0.590 (0.450) | **1.03** (0.220) | 0.660 (0.160) | 0.110 (0.034) |
| | 77 K | 0.240 (0.140) | 0.240 (0.190) | **0.420** (0.093) | 0.210 (0.062) | 0.031 (0.012) |
| $MoSe_2$ | 300 K | 1.39 (0.800) | **2.39** (0.810) | 1.66 (0.810) | 1.65 (0.810) | 0.290 (0.081) |
| | 150 K | 0.450 (0.310) | **1.06** (0.320) | 0.610 (0.320) | 0.570 (0.320) | 0.100 (0.033) |
| | 77 K | 0.130 (0.120) | **0.410** (0.120) | 0.220 (0.120) | 0.170 (0.120) | 0.030 (0.014) |
| $WS_2$ | 300 K | 1.52 (0.70) | 1.98 (0.720) | **2.03** (0.760) | 1.85 (0.760) | 0.280 (0.082) |
| | 150 K | 0.411 (0.280) | 0.613 (0.280) | **0.770** (.280) | 0.721 (0.350) | 0.104 (0.030) |
| | 77 K | 0.120 (0.110) | 0.181 (0.113) | 0.211 (0.113) | **0.271** (0.113) | 0.034 (0.012) |
| $WSe_2$ | 300 K | 1.88 (0.620) | **1.92** (0.620) | 1.44 (0.620) | 1.13 (0.620) | 0.260 (0.120) |
| | 150 K | 0.590 (0.220) | **0.750** (0.220) | 0.490 (0.220) | 0.380 (0.220) | 0.091 (0.032) |
| | 77 K | 0.180 (0.100) | **0.270** (0.100) | 0.170 (0.100) | 0.130 (0.100) | 0.031 (0.014) |

This article is copyrighted as indicated in the article. Reuse of AIP content is subject to the terms at: http://scitation.aip.org/termsconditions. Downloaded to IP: 147.8.204.164 On: Tue, 02 Dec 2014 09:15:56

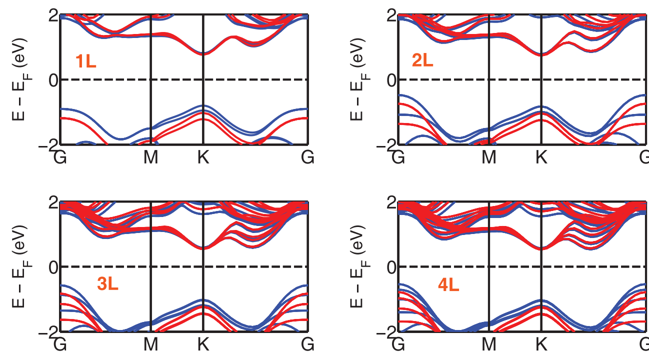


FIG. 7. *Ab initio* calculated electronic structure of $MoS_2$: 1L, 2L, 3L, and 4L structures using a PBE (blue) and hybrid HSE (red) functional. The HSE functional provides a correction to the underestimated PBE bandgap while the salient features of the electronic structure that would affect the density-of-modes calculation remain the same.

band edges, the HSE energies appear to be shifted with respect to the PBE energies. The effective masses for the HSE band structures are lower by up to 17% for the conduction band valleys at $K$ and $\Sigma$ and are lower by up to 11% for the valence band valleys at $K$ and $\Gamma$.

To verify that the HSE functional leaves the thermoelectric trends predicted from the PBE functional unchanged, we compute the density-of-modes and thermoelectric performance of 1L, 2L, and 3L $MoS_2$ using the HSE functional with the inclusion of spin orbit coupling. Figure 8 illustrates the DOM, Seebeck coefficient, power factor, and ZT for the 1L, 2L, and 3L structures of $MoS_2$ computed with the HSE functional. The quantitative values do differ. For the $MoS_2$ trilayer structure, the HSE (PBE) functionals give a peak n-type power factor of 0.41 (0.28) $WK^{-2}\,m^{-2}$ and a peak n-type ZT of 2.4 (2.2). However, the HSE results for few-layer $MoS_2$ structures demonstrate the same trends in the shape of the density of modes and the same trends in the values for the power factors and ZT. Both the HSE and PBE calculations show that the turn-on of the density of modes is sharpest for the tri-layer structure resulting in maximum values for the power factor and ZT. Since the primary effect on the low energy states of the exact exchange in the HSE functional is to shift the band edges with respect to those of a PBE calculation, the trends resulting from the shape of the density of modes should be preserved.

Figure 9 summarizes the values from the PBE calculations for the peak n-type and p-type ZT and power factors for each TMDC material and layer thickness. In the n-type $MoSe_2$, $WS_2$, and $WSe_2$ structures, the peak power-factor, and the peak ZT do not occur at the same film thickness. For example, in $MoSe_2$, a single monolayer has the highest power factor, and a bilayer has the highest ZT. This can be explained by the increase in the electronic thermal conductivity, $\kappa_e$ as the Fermi level is moved into the conduction band.

Figure 10 shows the ratio of the total thermal conductivity, $\kappa_{\mathrm{tot}}$, with respect to the lattice thermal conductivity, $\kappa_l$, for each TMDC material. The two guide lines on each figure illustrate the reduced Fermi level position at which the maximum n-type power factor and ZT occurs. The ratio $\kappa_{\mathrm{tot}}/\kappa_l = 1 + \kappa_e/\kappa_l$ is higher at the Fermi level position where the maximum power factor occurs. This increase in $\kappa_e$ explains why the peak power factor and ZT occur at different Fermi energies and film thicknesses.

A number of recent studies report on the theoretical[54,55] and experimental values[56,57] of the lattice thermal conductivity on monolayer and few-layer TMDC materials with values of $\kappa_l$ ranging from 19 $Wm^{-1}\,K^{-1}$ to 83 $Wm^{-1}\,K^{-1}$. Experimental measurements of the in-plane $\kappa_l$ in suspended samples of $MoS_2$[57] find a value of 34.5 $Wm^{-1}\,K^{-1}$ for 1L $MoS_2$ and 52 $Wm^{-1}\,K^{-1}$ for few-layer $MoS_2$. To assess whether the inequivalent $\kappa_l$ values for the monolayer and few-layer TMDC

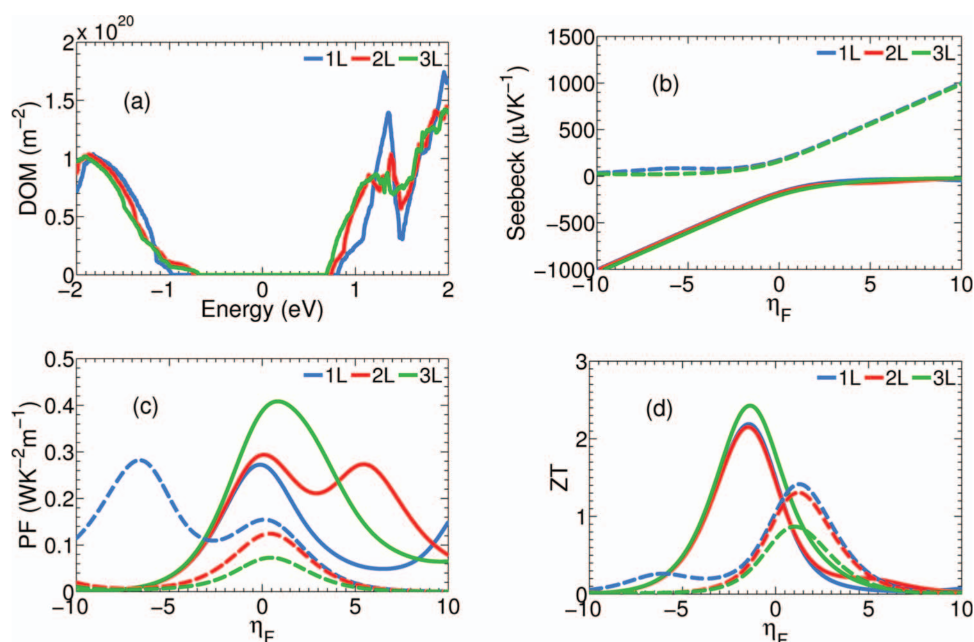


FIG. 8. HSE calculation of the (a) density-of-modes, (b) Seebeck coefficient, (c) Power factor, and (d) ZT 1L (blue), 2L (red), 3L (green) $MoS_2$. The n-type thermoelectric parameters are plotted with a solid line and the p-type parameters are plotted with a broken line as a function of the reduced Fermi energy, $\eta_F$.

This article is copyrighted as indicated in the article. Reuse of AIP content is subject to the terms at: http://scitation.aip.org/termsconditions. Downloaded to IP: 147.8.204.164 On: Tue, 02 Dec 2014 09:15:56

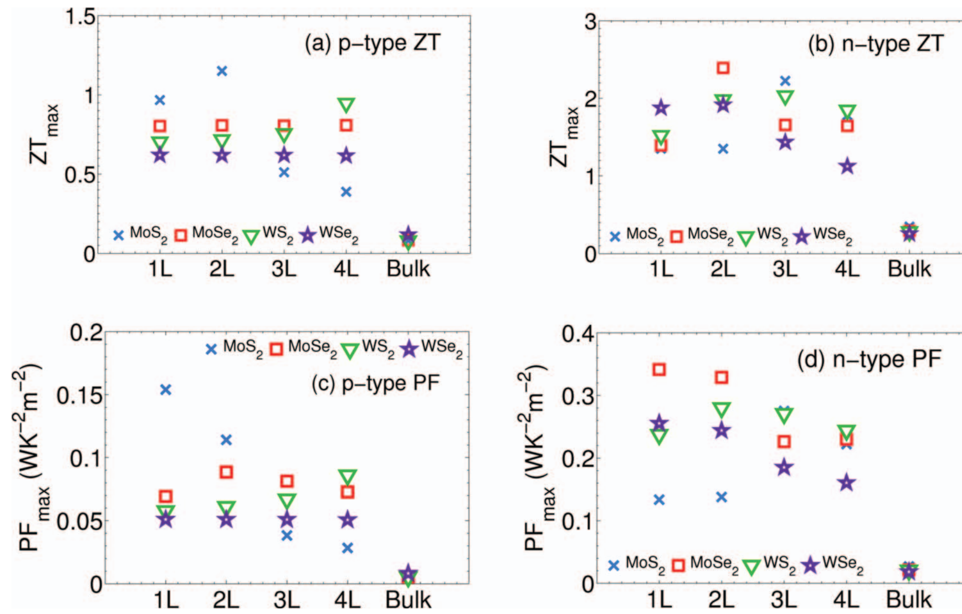


FIG. 9. Maximum thermoelectric performance for 1L (blue), 2L (red), 3L (green), 4L (purple), and bulk (black) $MoS_2$, $MoSe_2$, $WS_2$, $WSe_2$ at 300 K: (a) maximum p-type ZT, (b) maximum n-type ZT, (c) maximum p-type power factor, (d) maximum n-type power factor.

films leave the predicted thermoelectric trends unchanged, we computed the thermoelectric parameters using $\kappa_l = 34.5$ $\mathrm{Wm^{-1}\,K^{-1}}$ for the monolayer and $\kappa_l = 52$ $\mathrm{Wm^{-1}\,K^{-1}}$ for the few-layer TMDC films of each material. The values of ZT differ compared to using $\kappa_l = 19$ $\mathrm{Wm^{-1}\,K^{-1}}$ for each film thickness. For $MoS_2$, the room temperature n-type ZT values using the thickness dependent (constant) $\kappa_l$ for the 1L, 2L, 3L, and 4L structures are 0.87 (1.35), 0.63 (1.15), 1.11 (2.23), 0.89 (1.78). The maximum n-type ZT still occurs for the 3L structure and the minimum n-type ZT still occurs for the 1L structure. The trends for all of the n-type materials are preserved when a thickness dependent thermal conductivity is used. All of the values are shown in Fig. 11(b). For the n-type materials, changes in the density of modes are the dominant factor determining the trends. For p-type $MoSe_2$, $WS_2$, $WSe_2$, ZT varies little for different layer thicknesses when using a constant $\kappa_l$ as shown in Fig. 9(a). For p-type $MoS_2$, the difference between the maximum ZT of a bilayer and the second

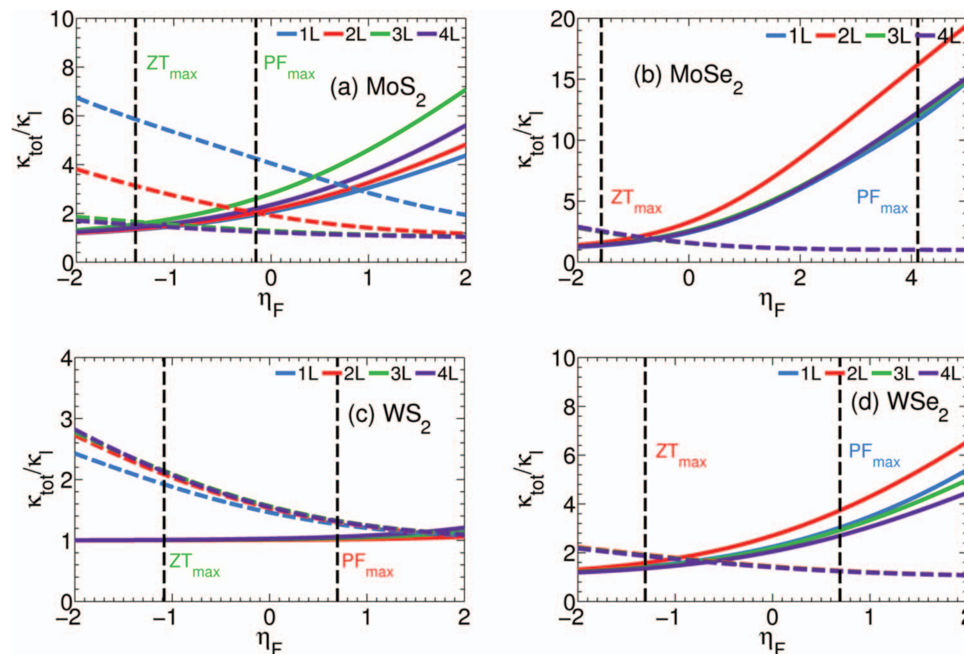


FIG. 10. Ratio of total thermal conductivity ($\kappa_l$+$\kappa_e$) over the lattice thermal conductivity ($\kappa_l$) at 300 K for (a) $MoS_2$, (b) $MoSe_2$, (c) $WS_2$, (d) $WSe_2$ for 1L (blue), 2L (red), 3L (green), and 4L (purple) structures. The n-type ratio is plotted with a solid line and p-type ratio with a broken line as a function of the reduced Fermi energy, $\eta_F$. The two vertical dashed lines show the reduced Fermi level position at which the maximum n-type power factor and ZT occur.

This article is copyrighted as indicated in the article. Reuse of AIP content is subject to the terms at: http://scitation.aip.org/termsconditions. Downloaded to IP: 147.8.204.164 On: Tue, 02 Dec 2014 09:15:56

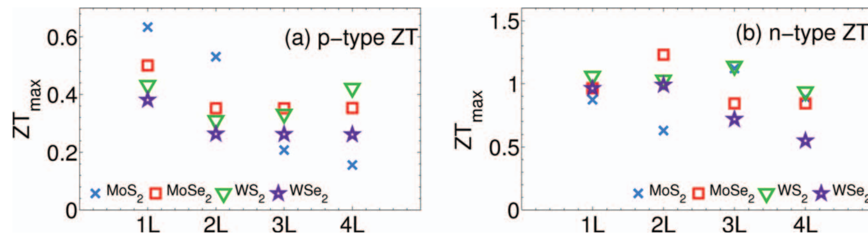


FIG. 11. Maximum ZT for (a) p-type and (b) n-type of $MoS_2$, $MoSe_2$, $WS_2$, $WSe_2$ at 300 K for 1L (blue), 2L (red), 3L (green), 4L (purple) structures accounting for thickness-dependent lattice thermal conductivity. $\kappa_l = 34.5$ Wm$^{-1}$ K$^{-1}$ used for the 1L structures and $\kappa_l = 52$ Wm$^{-1}$ K$^{-1}$ used for the few-layer structures.

highest value of a monolayer is small. Therefore, reducing the value of $\kappa_l$ for a monolayer from 52 to 35.4 WM$^{-1}$ K$^{-1}$ is sufficient to cause the peak value of ZT to occur at monolayer thickness for all 4 p-type materials as shown in Fig. 11(a).

In an attempt to study the transition of the thermoelectric performance from few-layer films to bulk like performance, we calculate the thermoelectric parameters for an 8L film of $WS_2$. Figure 12 illustrates the density of modes and the ZT for bulk, 3L and 8L $WS_2$. The n-type 0.974 ZT value of the 8L film is a factor of 1.9 smaller than that of the 4L film, but it is still a factor of 3.5 larger than that of the bulk. The p-type 0.163 ZT value of the 8L film is a factor of 4.7 smaller than that of the 4L film, and it is a factor of 2.0 larger that that of the bulk. Even at 8 monolayers, there is still an enhancement of the ZT value compared to that of the bulk, and the enhancement is larger in the n-type material.

The thermoelectric performance in the low dimensional structures is enhanced by the more abrupt step-like shape of the density of modes distribution.[34] It is clear from Eq. (4), that with $E_F \leq 0$, a step-function density of modes removes all negative contributions to the integrand of $I_1$ giving a maximum value for $I_1$. The conduction band DOM distribution for the maximum and minimum ZT structures for each material are plotted in Figure 13. In all cases, the DOM with the sharper turn-on at the band edge gives rise the maximum value for ZT.

## IV. DISCUSSION

The enhancement in the thermoelectric performance of *few* monolayer TMDC materials is in contrast to the enhanced thermoelectric performance observed for only a single quintuple (QL) layer of p-type $Bi_2Te_3$. Above 1 QL of $Bi_2Te_3$, the thermoelectric figure of merit approaches the bulk ZT.[16,17] The enhancement of ZT in n-type monolayer $Bi_2Te_3$ is minimal. This difference in the effect of layer thickness on ZT in the two different classes of materials can be explained by differences in the effect of thickness on the band-edge degeneracy and the density of modes. The valence band of monolayer $Bi_2Te_3$ is a ring in k-space that covers much of the Brillouin zone as shown in Fig. 4(d) of Ref. 17. Thus, the integration over $k_\perp$ in Eq. (7) jumps from zero in the bandgap to a finite number at the band edge resulting in a step-function turn-on of the valence band density of modes as seen in Fig. 3 of Ref. 16 and Fig. 2 of Ref. 17. The size of the ring in k-space quickly collapses for thicknesses above a monolayer, and the large enhancement in ZT dissappears. In a parabolic band, the band edge is a point in k-space, and, in two-dimensions, the density of modes turns on smoothly as $\sqrt{E}$.[34] The band edge of n-type monolayer $Bi_2Te_3$ remains parabolic resulting in a smooth turn-on of the density-of-modes and no significant enhancement of ZT.

The bands of the TMDC materials also remain parabolic at the band edges, however the conduction bands at the $K_c$ and the $\Sigma_c$ valleys become nearly degenerate for few monolayer thicknesses as shown in Fig. 1. Since the $\Sigma_c$ valley is 6-fold degenerate, and the $K_c$ valley is 2-fold degenerate, this results in a near 8-fold degeneracy of the conduction band edge. This increases the density of modes in the conduction band by a factor of 8 from that of a single valley. Furthermore, with increasing film thickness from 1L to 4L, the splitting of the $\Sigma_c$ bands resulting from interlayer coupling is on the order of $k_BT$. In $MoS_2$, the splitting at $\Sigma_C$ is 0.4 meV for the 2L and 40 meV for the 4L structure. The other materials show similar magnitudes of the energy splitting as a function of thickness. Therefore, the near-degeneracy of the bands at $\Sigma_c$ increases linearly with the film thickness, so that the number of modes

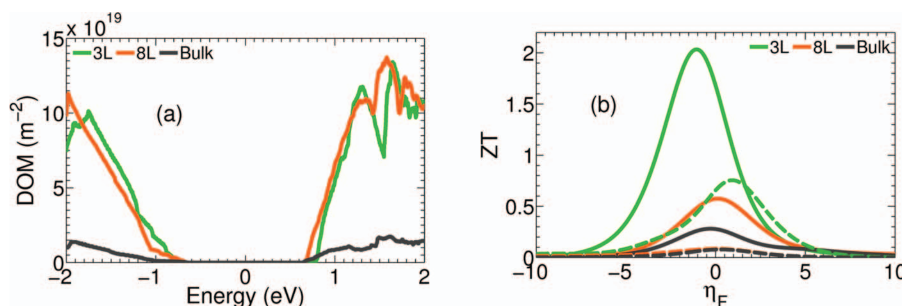


FIG. 12. (a) Density of modes and (b) ZT as a function of the reduced Fermi level for 3L (green), 8L (orange), and bulk (bulk) $WS_2$.

This article is copyrighted as indicated in the article. Reuse of AIP content is subject to the terms at: http://scitation.aip.org/termsconditions. Downloaded to IP: 147.8.204.164 On: Tue, 02 Dec 2014 09:15:56

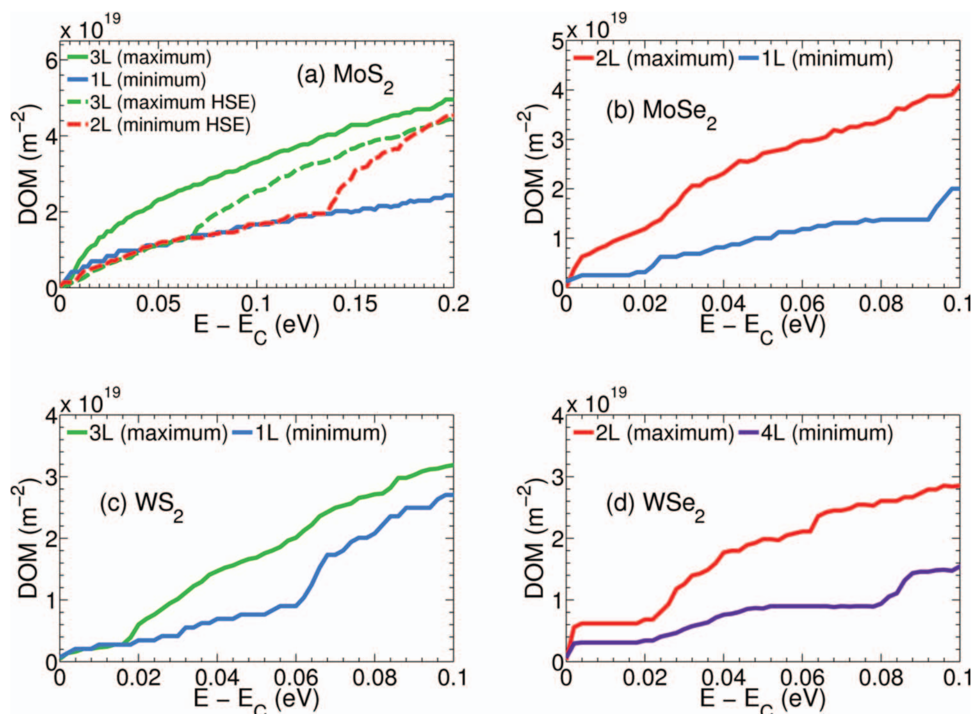


FIG. 13. Conduction band density of modes (DOM) for (a) $MoS_2$, (b) $MoSe_2$, (c) $WS_2$, and (d) $WSe_2$ at film thicknesses where the maximum and the minimum ZT occurs with respect to the energy away from the conduction band edge, $E_C$.

per layer becomes relatively insensitive to the layer thickness for few monolayer thicknesses.

The interlayer coupling of the out-of-plane $d_{z^2}$ and $p_z$ orbitals result in the strongest interlayer hybridization and energy level splitting.[58] In $MoS_2$ the orbital composition of the conduction band $\Sigma_c$ valley is 36% $d_{z^2}$, 22% $d_{xy}$, 23% $d_{x^2-y^2}$, 6% $p_z$, and 5% $p_x$ and $p_y$. The d-orbital composition of the $K_c$ valley is 67% $d_{z^2}$. With increasing layer number, the $K_c$ valley splitting is larger than $k_BT$ so that the number of modes contributed by the $K_c$ valleys remains 3 independent of layer number. Thus, when the $\Sigma_c$ valley falls within $k_BT$ of the $K_c$ valley, its contribution to the density of modes dominates for few-layer thicknesses. Beyond 4 layers, the total splitting becomes larger than 2 $k_BT$, and the number of accessible modes at $\Sigma_c$ no longer increases linearly with thickness.

Beyond a monolayer, the valence band shifts to $\Gamma_v$ for $MoS_2$, $MoSe_2$, and $WS_2$. The energy difference between $\Gamma_v$ and $K_v$ varies as a function of the film thickness and material. For $MoS_2$ the energy difference between $\Gamma_v$ and $K_v$ increases from 35 meV for the bilayer to 470 meV and 510 meV for the 3L and 4L structures, respectively. The near degeneracy of the $\Gamma_v$ and $K_v$ valleys leads to the largest p-type density of modes for 2L $MoS_2$. For $MoSe_2$, the $\Gamma_v$ and $K_v$ valleys are nearly degenerate above a single monolayer. In $WS_2$, the energy difference of the $\Gamma_v$ and $K_v$ valleys decreases from 42 meV to 21 meV as the film thickness is increased from a bilayer to four layers. For $WSe_2$, the valence band maxima continues to reside at $K_v$ beyond a monolayer. Once the valence band $K_v$ valleys begin to contribute in $MoSe_2$, $WS_2$, and $WSe_2$, the density of modes per layer becomes relatively independent of layer thickness, since there is little splitting of the $K_v$ valleys due to the interlayer coupling.[58] The $K_v$ valley orbital composition contains no $d_{z^2}$ or $p_z$ components. In $MoS_2$, the splitting varies from 0.2 meV for the 2L structure to 7.6 meV for the 4L structure. The other materials show similar magnitudes of the energy splitting as a function of thickness. Thus, at room temperature, the number of contributed modes per layer within $k_BT$ of the $K_v$ valley minimum remains constant for thicknesses in the range of one to four monolayers.

For the 8 layer $WS_2$ structure, the conduction band $K_c$ and $\Sigma_c$ valleys are still nearly degenerate. The $K_c$ valley lies 21 meV above the $\Sigma_c$ valley. However, at both valleys, the total splitting of the 8 bands contributed from the 8 layers is much greater than $k_BT$ at room temperature. At $\Sigma_c$, only two of the 8 bands are within 26 meV of the valley minimum. The overall energy splitting of the 8 bands at $\Sigma_c$ is 193 meV. In the valence band, the $K_v$ valley is 22 meV below the $\Gamma_v$ valley. However, the 8 bands from the 8 monolayers are split over a total range of 180 meV, and the second band is 40 meV below the $K_v$ valley maximum. Thus, as the number of layers increase, the total energy splitting of the bands contributed from each layer increases, and the number of modes per layer within $k_BT$ of the valley minimums decreases.

As the number of layers becomes macroscopic such that the crystal is periodic in all three dimensions, the total splitting of the bands evolves into the width of the dispersive band along $k_z$ for the bulk crystal. For bulk $WS_2$, the width of the band along the vertial $k_z$ direction from $\Sigma_c$ to $R$ at the top of the Brillouin zone is 208 meV which is 15 meV larger than the total splitting of the 8 layer stack. Furthermore, in the bulk, the $K_c$ valley is 126 meV above the $\Sigma_c$ minimum, so the $K_c$ contributes no modes to the density of modes near the conduction band edge. In the valence band, the $K_v$ valley maximum is 225 meV below the $\Gamma_v$ maximum, so that the density of

This article is copyrighted as indicated in the article. Reuse of AIP content is subject to the terms at: http://scitation.aip.org/termsconditions. Downloaded to IP: 147.8.204.164 On: Tue, 02 Dec 2014 09:15:56

modes near the valence band edge, is entirely from the $\Gamma_v$ valley. The lack of valley near-degeneracy and the width of the bulk dispersive bands along $k_z$, result in a minimum density of modes per layer near the band edges compared to those of few layer structures. The reduced number of modes per layer within $k_BT$ of the band edges results in reduced per-layer values of the thermoelectric figure of merit.

For both material systems $Bi_2Te_3$ and the semiconducting TMDCs, the enhancement of ZT results from the increased degeneracy or near-degeneracy of the band edges. The origin and nature of the degeneracy is different. In the $Bi_2Te_3$, the valence band edge becomes inverted into a ring as a result of the coupling of the topological surface states. In the TMDCs at few-layer thicknesses, different valleys become nearly degenerate. In the conduction band, the $\Sigma_c$ valleys become nearly degenerate with the $K_c$ valleys, and they contribute 6 more modes to the 2 modes from the $K_c$ valleys. In the valence band, the $K_v$ valleys become nearly degenerate with the $\Gamma_v$, and they contribute 2 more modes. Furthermore, because of the weak interlayer coupling at $K_v$ and $\Sigma_c$, the additional bands from additional layers lie within $k_BT$ of the band edges for few layers. The increased band-edge degeneracy results in a sharper turn-on of the density of modes and an increased value of ZT.

## V. SUMMARY

The electronic structure of one to four monolayers of the semiconducting transition metal dichalcogenides $MoS_2$, $MoSe_2$, $WS_2$, $WSe_2$ are calculated using DFT with spin-orbit coupling and the PBE functional. Comparisons are made to results in the absence of spin-orbit coupling, and the PBE results are compared to HSE calculations for $MoS_2$. The peak n-type value of ZT increases by a factor of 6–8 over the bulk value for all materials. Among the 4 materials and 4 thicknesses, bilayer $MoSe_2$ gives the maximum n-type ZT value of 2.4. The peak p-type value of ZT increases by a factor of 5–14 over the bulk value for all materials. The maximum p-type ZT value of 1.2 occurs for bilayer $MoS_2$. The maximum power factor generally occurs for a different layer thickness and at a more degenerate Fermi level than the maximum value of ZT. This difference can be explained by the increased electrical thermal conductivity at the Fermi level corresponding to the maximum power factor. For all materials, the maximum value of ZT coincides with the sharpest turn-on of the density of modes distribution at the band edge. The sharper turn-on is driven by the near valley degeneracy of the conduction band $K_c$ and $\Sigma_c$ valleys and the valence band $\Gamma_v$ and $K_v$ valleys. For few layer structures, the degeneracy is enhanced by the weak interlayer coupling at the $\Sigma_c$ and $K_v$ valleys.

## ACKNOWLEDGMENTS

This work is supported in part by the National Science Foundation (NSF) Grant Nos. 1124733 and 1128304 and the Semiconductor Research Corporation (SRC) Nanoelectronic Research Initiative as a part of the Nanoelectronics for 2020 and Beyond (NEB-2020) program, FAME, one of six centers of STARnet, a Semiconductor Research Corporation program sponsored by MARCO and DARPA, and the University Grant Council (Contract No. AoE/P-04/08) of the Government of HKSA (F.Z.). This work used the Extreme Science and Engineering Discovery Environment (XSEDE), which is supported by NSF, Grant No. OCI-1053575.

[1] B. Radisavljevic, A. Radenovic, J. Brivio, V. Giacometti, and A. Kis, Nat. Nanotechnol. **6**, 147 (2011).
[2] Y. Yoon, K. Ganapathi, and S. Salahuddin, Nano Lett. **11**, 3768 (2011).
[3] H. Fang, S. Chuang, T. C. Chang, K. Takei, T. Takahashi, and A. Javey, Nano Lett. **12**, 3788 (2012).
[4] K. Alam and R. K. Lake, IEEE Trans. Electron Devices **59**, 3250 (2012).
[5] A. N. Han Liu and P. Ye, ACS Nano **6**, 8563 (2012).
[6] T. Li and G. Galli, J. Chem. Phys. C **111**, 16192 (2007).
[7] D. Xiao, G.-B. Liu, W. Feng, X. Xu, and W. Yao, Phys. Rev. Lett. **108**, 196802 (2012).
[8] K. S. Novoselov and A. H. C. Neto, Physica Scr. **2012**, 014006.
[9] Q. H. Wang, K. Kalantar-Zadeh, A. Kis, J. N. Coleman, and M. S. Strano, Nat. Nanotech. **7**, 699 (2012).
[10] A. Geim and I. Grigorieva, Nature **499**, 419 (2013).
[11] M. Xu, T. Liang, M. Shi, and H. Chen, Chem. Rev. **113**, 3766 (2013).
[12] S. Z. Butler, S. M. Hollen, L. Cao, Y. Cui, J. A. Gupta, H. R. Gutirrez, T. F. Heinz, S. S. Hong, J. Huang, A. F. Ismach, *et al.*, ACS Nano **7**, 2898 (2013).
[13] Y. Sun, H. Cheng, S. Gao, Q. Liu, Z. Sun, C. Xiao, C. Wu, S. Wei, and Y. Xie, J. Am. Chem. Soc. **134**, 20294 (2012).
[14] V. Goyal, D. Teweldebrhan, and A. A. Balandin, Appl. Phys. Lett. **97**, 133117 (2010).
[15] P. Ghaemi, R. S. K. Mong, and J. E. Moore, Phys. Rev. Lett. **105**, 166603 (2010).
[16] F. Zahid and R. Lake, Appl. Phys. Lett. **97**, 212102 (2010).
[17] J. Maassen and M. Lundstrom, Appl. Phys. Lett. **102**, 093103 (2013).
[18] F. Zahid and R. K. Lake, personal communication (2011).
[19] A. Amara, Y. Frongillo, M. J. Aubin, S. Jandl, J. M. Lopez-Castillo, and J. P. Jay-Gerin, Phys. Rev. B **36**, 6415 (1987).
[20] H. Imai, Y. Shimakawa, and Y. Kubo, Phys. Rev. B **64**, 241104(R) (2001).
[21] H. Guo, T. Yang, P. Tao, Y. Wang, and Z. Zhang, J. Appl. Phys. **113**, 013709 (2013).
[22] M. Buscema, M. Barkelid, V. Zwiller, H. S. J. van der Zant, G. A. Steele, and A. Castellanos-Gomez, Nano Lett. **13**, 358–363 (2013).
[23] W. Huang, H. Da, and G. Liang, J. Appl. Phys. **113**, 104304 (2013).
[24] C. Lee, J. Hong, M.-H. Whangbo, and J. H. Shim, Chem. Mater. **25**, 3745 (2013).
[25] P. E. Blöchl, Phys. Rev. B **50**, 17953 (1994).
[26] J. P. Perdew, K. Burke, and M. Ernzerhof, Phys. Rev. Lett. **77**, 3865 (1996).
[27] M. Ernzerhof and G. E. Scuseria, J. Chem. Phys. **110**, 5029 (1999).
[28] G. Kresse and J. Hafner, Phys. Rev. B **48**, 13115 (1993).
[29] G. Kresse and J. Furthmuller, Comput. Mater. Sci. **6**, 15 (1996).
[30] S. Grimme, J. Comput. Chem. **27**, 1787 (2006).
[31] J. Heyd, G. E. Scuseria, and M. Ernzerhof, J. Chem. Phys. **118**, 8207 (2003).
[32] C. Jeong, R. Kim, M. Luisier, S. Datta, and M. Lundstrom, J. Appl. Phys. **107**, 023707 (2010).
[33] A. Paul, S. Salamat, C. Jeong, G. Klimeck, and M. Lundstrom, J. Comput. Electron. **11**, 56 (2012).
[34] R. Kim, S. Datta, and M. S. Lundstrom, J. Appl. Phys. **105**, 034506 (2009).
[35] R. Mansfield and S. A. Salam, Proc. Phys. Soc., London, Sect. B **66**, 377 (1953).
[36] S. Thakurta and A. Dutta, J. Phys. Chem. Solids **44**, 407 (1983).
[37] K. Kaasbjerg, K. S. Thygesen, and K. W. Jacobsen, Phys. Rev. B **85**, 115317 (2012).
[38] V. Varshney, S. S. Patnaik, C. Muratore, A. K. Roy, A. A. Voevodin, and B. L. Farmer, Comput. Mater. Sci. **48**, 101 (2010).
[39] C. Chiritescu, D. G. Cahill, N. Nguyen, D. Johnson, A. Bodapati, P. Keblinski, and P. Zschack, Science **315**, 351 (2007).
[40] K. Bronsema, J. De Boer, and F. Jellinek, Z. Anorg. Allg. Chem. **540**, 15 (1986).
[41] W. Schutte, J. D. Boer, and F. Jellinek, J. Solid State Chem. **70**, 207 (1987).
[42] K. K. Kam and B. A. Parkinson, J. Phys. Chem. **86**, 463 (1982).
[43] H. Jiang, J. Phys. Chem. C **116**, 7664 (2012).
[44] R. Coehoorn, C. Haas, J. Dijkstra, C. J. F. Flipse, R. A. de Groot, and A. Wold, Phys. Rev. B **35**, 6195 (1987).

This article is copyrighted as indicated in the article. Reuse of AIP content is subject to the terms at: http://scitation.aip.org/termsconditions. Downloaded to IP: 147.8.204.164 On: Tue, 02 Dec 2014 09:15:56

[45] L. Liu, S. Bala Kumar, Y. Ouyang, and J. Guo, IEEE Trans. Electron Devices **58**, 3042 (2011).
[46] A. Kuc, N. Zibouche, and T. Heine, Phys. Rev. B **83**, 245213 (2011).
[47] Y. Ding, Y. Wang, J. Ni, L. Shi, S. Shi, and W. Tang, Phys. B **406**, 2254 (2011).
[48] A. Ramasubramaniam, Phys. Rev. B **86**, 115409 (2012).
[49] K. F. Mak, C. Lee, J. Hone, J. Shan, and T. F. Heinz, Phys. Rev. Lett. **105**, 136805 (2010).
[50] T. Cheiwchanchamnangij and W. R. Lambrecht, Phys. Rev. B **85**, 205302 (2012).
[51] H. Shi, H. Pan, Y.-W. Zhang, and B. I. Yakobson, Phys. Rev. B **87**, 155304 (2013).
[52] P. Pichanusakorn and P. R. Bandaru, Appl. Phys. Lett. **94**, 223108 (2009).
[53] F. Zahid, L. Liu, Y. Zhu, J. Wang, and H. Guo, AIP Adv. **3**, 052111 (2013).
[54] W. Li, J. Carrete, and N. Mingo, Appl. Phys. Lett. **103**, 253103 (2013).
[55] Y. Cai, J. Lan, G. Zhang, and Y.-W. Zhang, Phys. Rev. B **89**, 035438 (2014).
[56] C. Muratore, V. Varshney, J. J. Gengler, J. J. Hu, J. E. Bultman, T. M. Smith, P. J. Shamberger, B. Qiu, X. Ruan, A. K. Roy, *et al.*, Appl. Phys. Lett. **102**, 081604 (2013).
[57] R. Yan, J. R. Simpson, S. Bertolazzi, J. Brivio, M. Watson, X. Wu, A. Kis, T. Luo, A. R. Hight Walker, and H. G. Xing, ACS Nano **8**, 986 (2014).
[58] H.-P. Komsa and A. V. Krasheninnikov, Phys. Rev. B **88**, 085318 (2013).
[59] H. Zeng, G.-B. Liu, J. Dai, Y. Yan, B. Zhu, R. He, L. Xu, S. Xu, X. Chen, and X. Cui, Nat. Sci. Rep. **3**, 1608 (2013).

This article is copyrighted as indicated in the article. Reuse of AIP content is subject to the terms at: http://scitation.aip.org/termsconditions. Downloaded to IP: 147.8.204.164 On: Tue, 02 Dec 2014 09:15:56